SEECCM III
3rd South-East European Conference on Computational Mechanics-
an ECCOMAS and IACM Special Interest Conference
M. Papadrakakis, M. Kojic, I. Tuncer (eds.)
Kos Island, Greece, 12–14 June 2013

SECOND ORDER GODUNOV SPH FOR HIGH VELOCITY IMPACT DYNAMICS

A. Connolly[1], L. Iannucci[1], R. Hillier[1] and D. Pope[2]

[1]Department of aeronautics
Imperial College London
South Kensington Campus
SW7 2AZ
e-mail: a.connolly08@imperial.ac.uk

[2] Defence Science and Technology Labs
Dstl Porton Down
Wiltshire
SP4 0JQ
e-mail: djpope@dstl.gov.uk

Keywords: SPH, Godunov, Riemann, MUSCL, high-velocity, impact

Abstract. *In this work the Godunov Smoothed Particle Hydrodynamics (SPH) method for material with strength is extended to second order in space. This is achieved by separating the continuum equations of motion into their constituent hydrodynamic and deviatoric parts and using a MUSCL-type reconstruction and limiting procedure for the left and right Riemann states. The split equations are then advanced in time sequentially using a first-order operator splitting procedure. The resulting equations require no user defined artificial damping parameters as sufficient numerical dissipation is introduced through the use of a Riemann solver. One and two dimensional elastic-plastic flows are chosen to demonstrate the efficacy of the proposed formulation and the results are compared with exact solutions, the original first order scheme and the standard artificial viscosity SPH scheme. The new method is then applied to the simulation of a representative ballistic impact on a ceramic armour material.*

1 INTRODUCTION

Traditionally in SPH the shock is smeared by applying an artificial viscosity [22] term to the momentum and energy equations. Several forms of artificial viscosity have been described in the literature [9, 22, 1] with the most common implementation (found in most SPH codes) being that of Monaghan *et al.* [22]. When using the artificial viscosity without special treatments [27, 4], care must be taken not to introduce excessive artificial smoothing into smooth regions away from the shock. This may be achieved by a time-consuming trial-and-error analysis [28] which may be very undesirable for the user.

The Godunov reformulation of the SPH equations have been developed [33, 12, 23] whereby the Riemann problem is solved between the two interacting particles. The solution of the Riemann problem in Lagrangian coordinates provides the post wave-breakup pressure and velocity at the interface between two interacting particles which introduces sufficient numerical dissipation for stable integration. The advantage of these Godunov reformulations is that no user-defined damping parameters or associated sensitivity analyses are required; sufficient damping is automatically introduced into the solution. The strictly conservative Godunov SPH method developed by Inutsuka (2002) [12] was developed for inviscid fluid simulations and maintains second-order spatial accuracy in smooth regions by a reconstruction procedure. The Godunov SPH method of Parshikov *et al.* (2002) [23] was developed for fluid and solid dynamics and is first-order accurate everywhere in the solution. This work presents an extension of the Parshikov *et al.* scheme for fluid and solid-dynamics to second-order in space, while ensuring exact conservation of energy. This is done by splitting the integration procedure into a hydrodynamic and a deviatoric step, thereby removing the complications caused by the material strength as described in [10] for a free-Lagrange Voronoi tesselation method. The Lie-Trotter splitting is used which is first-order in time.

The new method is derived in Section 3.3 and tests for one and two-dimensional solid-dynamics are presented in Section 4. Section 5 applies the new scheme to a representative ballistic impact simulation and Section 6 concludes the work.

1.1 Motivation

The effective viscosity of the Parshikov *et al.* scheme [23] is shown to be high, which is a direct consequence of the use of a first-order Godunov scheme [30]. A piecewise linear reconstruction of the (primitive variables in the inviscid-fluid case) field variables to the contact surface between particles i and j, before invoking the Riemann solution, extends the spatial order of accuracy to $2^{\text{nd}}\ \mathcal{O}$ [32]. This is readily achieved using the SPH smoothed approximation of the gradient, as done in [33, 12]. Godunov's Theorem states that monotone linear schemes (having the property of not generating new extrema) for solving partial differential equations, can be at most first-order accurate [8]. Therefore, in order to achieve high-order spatial accuracy, without introducing new extrema which may lead to oscillations, a non-linear scheme must be used. This can be achieved using slope limiting procedures [30]. Such a scheme has high-order spatial accuracy in smooth regions of the solution but falls to low, or first order accuracy, in the vicinity of strong gradients or discontinuities. When considering the Cauchy stress tensor, its gradient results in a third-order tensor field (the implementation of which in three dimensions requires 18 elements per particle). This memory and computational requirement has meant that the Godunov SPH scheme for materials with strength has remained $1^{\text{st}}\ \mathcal{O}$ accurate in space. This work, then, is an attempt to remove the complication of the extension to 2^{nd} $\mathcal{O}$ of the Godunov SPH scheme caused by the inclusion of material strength.

2 SPH THEORY

The basis of the SPH method is in the approximation of a function of spatial coordinates $f(\boldsymbol{x})$ through the approximate kernel interpolation of the function at locations surrounding the point of interest. The usual derivation [21] is to start with the identity

$$f(\boldsymbol{x}) = \int f(\boldsymbol{x'})\delta\left(\boldsymbol{x} - \boldsymbol{x'}\right) d\boldsymbol{x'}. \tag{1}$$

The delta function is replaced by some smoothing (or "kernel") function $W(\boldsymbol{x} - \boldsymbol{x'}, h)$ with the same property as the delta function as the smoothing length h tends to zero:

$$\lim_{h\to 0} W(\boldsymbol{x} - \boldsymbol{x'}, h) = \delta(\boldsymbol{x} - \boldsymbol{x'}). \tag{2}$$

This gives the kernel approximation

$$f(\boldsymbol{x}) \approx \int f(\boldsymbol{x'})W\left(\boldsymbol{x} - \boldsymbol{x'}, h\right) d\boldsymbol{x'}. \tag{3}$$

The kernel function should satisfy the unity condition

$$\int W\left(\boldsymbol{x} - \boldsymbol{x'}, h\right) d\boldsymbol{x'} = 1 \tag{4}$$

and, in order to be computationally tractable, should be compact such that

$$W\left(\boldsymbol{x} - \boldsymbol{x'}, h\right) = 0 \quad \text{if} \quad |\boldsymbol{x} - \boldsymbol{x'}| \geq \kappa h \tag{5}$$

where κ is some scaling factor. For each particle with a mass m_i and mass density ρ_i, noting that $d\boldsymbol{x'}$ denotes the integration volume (in three dimensions), equation (3) may be discretized as the Riemann summation

$$f(\boldsymbol{x}) \approx \sum_j \frac{m_j}{\rho_j} f(\boldsymbol{x}_j)W\left(\boldsymbol{x} - \boldsymbol{x}_j, h\right). \tag{6}$$

If the function is taken as the density field ρ, the SPH summation approximation of the density is obtained:

$$\rho(\boldsymbol{x}) \approx \sum_j m_j W\left(\boldsymbol{x} - \boldsymbol{x}_j, h\right). \tag{7}$$

It is clear from equation (7) that the kernel function should satisfy some physically intuitive properties, such as being non-negative, and monotonically decreasing as $h \to 0$. For this reason, a Gaussian, or Gaussian-like function is commonly chosen as the kernel. The derivative of a function may be obtained by using integration by parts and the divergence theorem to give

$$\nabla f(\boldsymbol{x}) \approx \int_S f(\boldsymbol{x'})W(\boldsymbol{x} - \boldsymbol{x'}, h)\boldsymbol{n} dS - \int_\Omega f(\boldsymbol{x'})\nabla W(\boldsymbol{x} - \boldsymbol{x'}, h) d\boldsymbol{x'}. \tag{8}$$

In general, the surface integral in equation (8) is neglected in the actual computation as it vanishes if the kernel support does not intersect the boundary of the material domain. For simulations involving free-surfaces, the neglect of the surface integral contributes to the boundary deficiency in the SPH method. As the continuum equations of motion are first-order, equation (8) may be used to discretize the governing equations. Neglecting the surface integral, in one dimension, the errors in (8) may be estimated by taking the Taylor-series expansion around $\boldsymbol{x'}$ to give

$$\begin{aligned}\nabla f(\boldsymbol{x}) = -\int \Big[& f(\boldsymbol{x}) + (\boldsymbol{x}-\boldsymbol{x'})f'(\boldsymbol{x}) + \frac{(\boldsymbol{x}-\boldsymbol{x'})^2}{2!} f''(\boldsymbol{x}) + \\ & \mathcal{O}\left((\boldsymbol{x}-\boldsymbol{x'})^3\right) + \ldots \Big] \nabla W(\boldsymbol{x}-\boldsymbol{x'},h) d\boldsymbol{x'} \\ = \nabla f(\boldsymbol{x}) + & \frac{f''(\boldsymbol{x})}{2} \int (\boldsymbol{x}-\boldsymbol{x'})^2 \nabla W(\boldsymbol{x}-\boldsymbol{x'},h) d\boldsymbol{x'} + \\ & \mathcal{O}\left((\boldsymbol{x}-\boldsymbol{x'})^3\right).\end{aligned} \tag{9}$$

In (9) the second term in the Taylor expansion vanishes as, for even kernels $\int \nabla W d\boldsymbol{x'} = 0$. Therefore, the order of accuracy of the kernel approximation of the gradient is second-order, with errors of $\mathcal{O}(h^2)$. Similarly, the errors in the discrete approximation of (9) are of $\mathcal{O}(h^2)$ [25].

3 GOVERNING EQUATIONS

In the absence of body forces, the conservation equations for elastic flow are given as follows

$$\begin{aligned}\frac{D\rho}{Dt} &= -\rho \nabla \cdot \boldsymbol{v} \\ \frac{D\boldsymbol{v}}{Dt} &= \frac{1}{\rho} \nabla \cdot \boldsymbol{\sigma} \\ \frac{Du}{Dt} &= -\frac{\boldsymbol{\sigma}}{\rho} : \nabla \boldsymbol{v},\end{aligned} \tag{10}$$

where D/Dt is the substantial derivative and ρ, $\boldsymbol{v}$, u and $\boldsymbol{\sigma}$ are the material density, velocity, specific internal energy and Cauchy stress tensor respectively. The separation of the stress tensor into its dilatational and deviatoric components is assumed [35]

$$\boldsymbol{\sigma} = \boldsymbol{\tau} - P\boldsymbol{I}, \tag{11}$$

where $\boldsymbol{I}$ is the identity matrix.

3.1 Discretization

The variationally consistent discrete SPH equations [3] corresponding to (10) are given as [3]

$$\begin{aligned}\frac{D\rho_i}{Dt} &= \rho_i \sum_j \frac{m_j}{\rho_j} (\boldsymbol{v}_i - \boldsymbol{v}_j) \cdot \nabla_i W_{ij} \\ \frac{D\boldsymbol{v}_i}{Dt} &= \sum_j m_j \left(\frac{\boldsymbol{\sigma}_i + \boldsymbol{\sigma}_j}{\rho_i \rho_j} \right) \nabla_i W_{ij} \\ \frac{Du_i}{Dt} &= \frac{1}{2} \sum_j m_j \left(\frac{\boldsymbol{\sigma}_i + \boldsymbol{\sigma}_j}{\rho_i \rho_j} \right) (\boldsymbol{v}_i - \boldsymbol{v}_j) \cdot \nabla_i W_{ij},\end{aligned} \tag{12}$$

where the derivative of the kernel function $\nabla_i W_{ij}$ is defined as

$$\begin{aligned}\nabla_i W_{ij} =& \frac{\partial}{\partial \boldsymbol{x}_i} W\left(\boldsymbol{x}_i - \boldsymbol{x}_j, h\right) \\ =& \frac{\boldsymbol{x}_i - \boldsymbol{x}_j}{|\boldsymbol{x}_i - \boldsymbol{x}_j|} \frac{\partial W\left(|\boldsymbol{x}_i - \boldsymbol{x}_j|, h\right)}{\partial\left|\boldsymbol{x}_i - \boldsymbol{x}_j\right|} \\ =& -\nabla_j W_{ij}.\end{aligned} \tag{13}$$

3.2 Godunov reformulation of Parshikov *et al.*

In 2002 Parshikov *et al.* [23] directly introduced the Riemann solution to the SPH equations (12) by resolving the stresses and velocities along the vector of interaction and making the substitutions

$$\begin{aligned}P^*_{ij} &\leftarrow \frac{1}{2}\left(P_i + P_j\right) \\ v^*_{ij} &\leftarrow \frac{1}{2}\left(v^R_i + v^R_j\right) \\ \sigma^*_{ij} &\leftarrow \frac{1}{2}\left(\sigma^R_i + \sigma^R_j\right),\end{aligned} \tag{14}$$

where $v^R_{i,j} = \boldsymbol{v}_{i,j} \cdot \boldsymbol{e}_{ij}$, $\sigma^R_{i,j} = \boldsymbol{\sigma}^{x,y,z}_{i,j} \cdot \boldsymbol{e}_{ij}$ and the unit vector of interaction $\boldsymbol{e}_{ij} = \boldsymbol{x}_i - \boldsymbol{x}_j / |\boldsymbol{x}_i - \boldsymbol{x}_j|$. The substitution for the stresses requires the rotation of the stress tensor to the coordinate system $\boldsymbol{e}_{R,S,T}$ orthogonal to the vector of interaction $\boldsymbol{e}_{ij}$. The values with the star superscripts are not calculated using (14); instead the approximate acoustic wave primitive variable Riemann solver [30] is used to calculate the value of the stress and velocity in the star region in the three directions corresponding to $\boldsymbol{e}_{R,S,T}$ by

$$\begin{aligned}v^{*R}_{ij} &= \frac{v^R_j \rho_j c^l_j + v^R_i \rho_i c^l_i + \sigma^{RR}_j - \sigma^{RR}_i}{\rho_i c^l_i + \rho_j c^l_j} \\ \sigma^{*R}_{ij} &= \frac{\sigma^{RR}_j \rho_i c^l_i + \sigma^{RR}_i \rho_j c^l_j + \rho_i c^l_i \rho_j c^l_j \left(v^R_j - v^R_i\right)}{\rho_i c^l_i + \rho_j c^l_j} \\ v^{*S}_{ij} &= \frac{v^S_j \rho_j c^t_j + v^S_i \rho_i c^t_i + \sigma^{SR}_j - \sigma^{SR}_i}{\rho_i c^t_i + \rho_j c^t_j} \\ \sigma^{*S}_{ij} &= \frac{\sigma^{RS}_j \rho_i c^t_i + \sigma^{RS}_i \rho_j c^t_j + \rho_i c^t_i \rho_j c^t_j \left(v^S_j - v^S_i\right)}{\rho_i c^t_i + \rho_j c^t_j} \\ v^{*T}_{ij} &= \frac{v^T_j \rho_j c^t_j + v^T_i \rho_i c^t_i + \sigma^{TR}_j - \sigma^{TR}_i}{\rho_i c^t_i + \rho_j c^t_j} \\ \sigma^{*T}_{ij} &= \frac{\sigma^{RT}_j \rho_i c^t_i + \sigma^{RT}_i \rho_j c^t_j + \rho_i c^t_i \rho_j c^t_j \left(v^T_j - v^T_i\right)}{\rho_i c^t_i + \rho_j c^t_j}.\end{aligned} \tag{15}$$

In (15) c^l and c^t are the longitudinal and transverse wave speeds respectively. The resulting SPH equations are stated as

$$\begin{aligned}\frac{D\rho_i}{Dt} &= 2\rho_i \sum_j \frac{m_j}{\rho_j} \left(v_{ij}^{*R} - v_i^R\right) \boldsymbol{e}_{ij} \cdot \nabla_i W_{ij} \\ \frac{D\boldsymbol{v}_i}{Dt} &= 2 \sum_j m_j \frac{\sigma_{ij}^{*R}}{\rho_i \rho_j} \boldsymbol{e}_{ij} \nabla_i W_{ij} \\ \frac{Du_i}{Dt} &= 2 \sum_j m_j \frac{\sigma_{ij}^{*R}}{\rho_i \rho_j} \left(v_{ij}^{*R} - v_i^R\right) \boldsymbol{e}_{ij} \cdot \nabla_i W_{ij}.\end{aligned} \tag{16}$$

The algorithm presented in [23] corresponds to a spatially 1^{st} $\mathcal{O}$ Godunov method for solid mechanics and will form the basis of the work presented in forthcoming chapters. It is well known that the 1^{st} $\mathcal{O}$ Godunov method is highly diffusive, which is accentuated by the smoothing introduced by the SPH method. This is discussed in [23].

3.3 Second-order extension

In order to simplify the extension of the Godunov SPH method for materials with strength to second-order, it is proposed that the hydrodynamic and deviatoric parts of the stress tensor be used to sequentially and separately advance the density, velocity and specific internal energy in time. The SPH momentum and energy equations (12) are split into their constituent hydrodynamic and deviatoric parts as

$$\begin{aligned}\frac{D\boldsymbol{v}_i}{Dt} &= \sum_j m_j \left(\frac{\boldsymbol{\tau}_i + \boldsymbol{\tau}_j}{\rho_i \rho_j} - \boldsymbol{I}\frac{P_i + P_j}{\rho_i \rho_j}\right) \nabla_i W_{ij} \\ \frac{Du_i}{Dt} &= \frac{1}{2} \sum_j m_j \left(\frac{\boldsymbol{\tau}_i + \boldsymbol{\tau}_j}{\rho_i \rho_j} - \boldsymbol{I}\frac{P_i + P_j}{\rho_i \rho_j}\right) (\boldsymbol{v}_j - \boldsymbol{v}_i) \cdot \nabla_i W_{ij},\end{aligned} \tag{17}$$

where the first term in the brackets on the right hand side corresponds to the deviatoric part and the second term corresponds to the hydrodynamic part. The integration procedure is then split into the constituent hydrodynamic and deviatoric stages using Lie-Trotter splitting. The general form of splitting is

$$\frac{\partial f(t)}{\partial t} = Af(t) + Bf(t) \tag{18}$$

where $f(t)$ is some field-variable and A and B are linear differential operators corresponding to the deviatoric and hydrodynamic operations respectively. The sequential splitting algorithm is as follows

$$\begin{aligned}\frac{\partial x(t)}{\partial t} &= Ax(t), \quad t \in [t^n, t^{n+1}] \quad \text{where} \quad x(t^n) = f(t^n) \\ \frac{\partial y(t)}{\partial t} &= By(t), \quad t \in [t^n, t^{n+1}] \quad \text{where} \quad y(t^n) = x(t^{n+1})\end{aligned} \tag{19}$$

and the recombination of the split solution is given as $y(t^{n+1}) \approx f(t^{n+1})$. The splitting error is first-order in time and can be found by combining the Taylor series expansions of the two split functions $x(t)$ and $y(t)$ and taking the difference with the Taylor series expansion of the un-split function around point $f(t^n) = f_n$. Applying this splitting algorithm to the SPH momentum and energy equations (17) gives

$$\begin{aligned}
\frac{D\tilde{\boldsymbol{v}}_i}{Dt} &= \sum_j m_j \left(\frac{\boldsymbol{\tau}_i + \boldsymbol{\tau}_j}{\rho_i \rho_j}\right) \cdot \nabla_i W_{ij}, \text{ where } \tilde{\boldsymbol{v}}_i(t^n) = \boldsymbol{v}_i(t^n) \\
\frac{D\check{\boldsymbol{v}}_i}{Dt} &= -\sum_j m_j \left(\frac{P_i + P_j}{\rho_i \rho_j}\right) \nabla_i W_{ij}, \text{ where } \check{\boldsymbol{v}}_i(t^n) = \tilde{\boldsymbol{v}}_i(t^{n+1}) \\
\frac{D\tilde{u}_i}{Dt} &= \frac{1}{2}\sum_j m_j \left(\frac{\boldsymbol{\tau}_i + \boldsymbol{\tau}_j}{\rho_i \rho_j}\right) (\boldsymbol{v}_j - \boldsymbol{v}_i) \cdot \nabla_i W_{ij}, \text{ where } \tilde{u}_i(t^n) = u_i(t^n) \\
\frac{D\check{u}_i}{Dt} &= -\frac{1}{2}\sum_j m_j \left(\frac{P_i + P_j}{\rho_i \rho_j}\right) (\tilde{\boldsymbol{v}}_j - \tilde{\boldsymbol{v}}_i) \cdot \nabla_i W_{ij}, \text{ where } \check{u}_i(t^n) = \tilde{u}_i(t^{n+1}),
\end{aligned} \tag{20}$$

where $\tilde{\boldsymbol{v}}_i = \boldsymbol{v}_i^n + \Delta\tilde{\boldsymbol{v}}_i$. In order to obtain sufficient numerical dissipation, the hydrodynamic terms are replaced with the Godunov SPH equations of Parshikov *et al.* [23] for an inviscid, non-radiating fluid to get

$$\begin{aligned}
\frac{D\tilde{\boldsymbol{v}}_i}{Dt} &= \sum_j m_j \left(\frac{\boldsymbol{\tau}_i + \boldsymbol{\tau}_j}{\rho_i \rho_j}\right) \cdot \nabla_i W_{ij}, \text{ where } \tilde{\boldsymbol{v}}_i(t^n) = \boldsymbol{v}_i(t^n) \\
\frac{D\check{\boldsymbol{v}}_i}{Dt} &= -2\sum_j m_j \left(\frac{P_{ij}^*}{\rho_i \rho_j}\right) \nabla_i W_{ij}, \text{ where } \check{\boldsymbol{v}}_i(t^n) = \tilde{\boldsymbol{v}}_i(t^{n+1}) \\
\frac{D\tilde{u}_i}{Dt} &= \frac{1}{2}\sum_j m_j \left(\frac{\boldsymbol{\tau}_i + \boldsymbol{\tau}_j}{\rho_i \rho_j}\right) (\boldsymbol{v}_j - \boldsymbol{v}_i) \cdot \nabla_i W_{ij}, \text{ where } \tilde{u}_i(t^n) = u_i(t^n) \\
\frac{D\check{u}_i}{Dt} &= -2\sum_j m_j \left(\frac{P_{ij}^*}{\rho_i \rho_j}\right) \left(\tilde{v}_{ij}^* \boldsymbol{e}_{ij} - \tilde{\boldsymbol{v}}_i\right) \cdot \nabla_i W_{ij}, \text{ where } \check{u}_i(t^n) = \tilde{u}_i(t^{n+1}),
\end{aligned} \tag{21}$$

where P_{ij}^* and $\tilde{v}_{ij}^*$ are the pressure and velocity solutions of the Riemann-problem for the longitudinal wave-system. Note that, in contrast to the scheme of Parshikov *et al.* the Riemann problem needs only to be solved for the longitudinal wave system and no transformation of the stress-tensor is required. No dissipation is added to the deviatoric step of the split integration procedure and the spatial accuracy of the deviatoric momentum equation is second-order. By definition, the density is assumed to only change due to changes in volume, therefore the continuity equation is computed only in the hydrodynamic step. The continuity equation of Parshikov *et al.* [23] may be used

$$\frac{D\rho_i}{Dt} = 2\rho_i \sum_j \frac{m_j}{\rho_j} \left(\tilde{v}_{ij}^* \boldsymbol{e}_{ij} - \tilde{\boldsymbol{v}}_i\right) \cdot \nabla_i W_{ij}. \tag{22}$$

3.3.1 MUSCL-type reconstruction

To extend the hydrodynamic step in (21) to second-order, a linear reconstruction of the left and right states of the Riemann problem is used as first proposed for SPH in [11]. Using the SPH approximation of the gradient of a function, and taking into account the domain of influence, the reconstruction of the left and right hand Riemann states is written as

$$
\begin{aligned}
f_R &= f(\boldsymbol{x}_i) - \frac{r_{ij}}{2} \nabla f(\boldsymbol{x}_i)_{mon} \cdot \boldsymbol{e}_{ij} \left[1 - c_i \Delta t\right] \\
f_L &= f(\boldsymbol{x}_j) + \frac{r_{ij}}{2} \nabla f(\boldsymbol{x}_j)_{mon} \cdot \boldsymbol{e}_{ij} \left[1 - c_j \Delta t\right],
\end{aligned}
\tag{23}
$$

where $r_{ij} = |\boldsymbol{x}_i - \boldsymbol{x}_j|$, $c_{i,j}$ is the longitudinal sound speed at the particle's position and Δt is the current time-step. In order to satisfy the monotonicity constraint at the shock [8], the gradients of the primitive variables must be modified such that the first-order method is recovered. In [12] this is done by setting the gradients to zero when the interacting particles are approaching each other at a velocity close to the minimum wave speed of either interacting particles. A more advanced technique to automatically fulfill the monotonicity constraint by modifying the local gradient based on some sort of smoothness indicator, such as the ratio of successive gradients, as in [32]. This may be done by using one of a variety of different slope-limiter functions [30]. The resolved gradient

$$
\Delta Q = \nabla Q \cdot \boldsymbol{e}_{ij} \tag{24}
$$

is defined for particles i and j and the ratio of successive gradients r is defined as

$$
\begin{aligned}
r_i &= \frac{\Delta Q_j}{\Delta Q_i} \\
r_j &= \frac{\Delta Q_i}{\Delta Q_j} = \frac{1}{r_i}.
\end{aligned}
\tag{25}
$$

The chosen slope-limiter function $\phi(r)$ can then be used to construct the monotonized slopes

$$
\begin{aligned}
\nabla f(\boldsymbol{x}_i)_{mon} &= \phi(r_i) \nabla f(\boldsymbol{x}_i) \\
\nabla f(\boldsymbol{x}_j)_{mon} &= \phi(r_j) \nabla f(\boldsymbol{x}_j),
\end{aligned}
\tag{26}
$$

and using equation (23) the left and right Riemann states may be reconstructed. The following 2nd $\mathcal{O}$ Total Variation Diminishing (TVD) slope limiters [30] were implemented due to their symmetry preserving features ($\phi(r) = 1/\phi(r)$)

$$
\begin{aligned}
\phi(r)_{mc} &= \max\left(0, \min\left(2r,\ \frac{1+r}{2},\ 2\right)\right) \\
\phi(r)_{sw} &= \max\left(0,\ \min\left(\beta r,\ 1\right),\ \min(r,\ \beta)\right), \quad 1 \leq \beta \leq 2 \\
\phi(r)_{vl} &= \frac{r + |r|}{1 + |r|},
\end{aligned}
\tag{27}
$$

where the subscripts mc, sw and vl stand for Monotonized Central, Sweby and van Leer limiters respectively. Setting the $\beta = 1$ and $\beta = 2$ in the Sweby limiter gives the *minmod* and *superbee* limiters of Roe [30], respectively. It was found that the *superbee* limiter performed well; it is used in all the 2nd $\mathcal{O}$ simulations in this work.

3.4 Conservation

In order to conserve energy exactly in the split integration procedure, the energy equations (21) are modified. As in [12], the appropriate time-centering of the velocity field is used, along with the anti-symmetric nature of the kernel derivative (13), to obtain an expression which vanishes for the sum over all pairs of interacting particles. The total energy at time $t = t^n$ is defined as (the sum of the kinetic and internal energies)

$$E^n = \sum_i m_i \left(\frac{1}{2} (\boldsymbol{v}_i^n)^2 + u_i^n \right). \tag{28}$$

For energy to be conserved, the total energy must remain constant over the time-step ($\Delta E = E^{n+1} - E^n = 0$)

$$\Delta E = \sum_i m_i \left(\frac{1}{2} (\boldsymbol{v}_i^{n+1})^2 + u_i^{n+1} - \frac{1}{2} (\boldsymbol{v}_i^n)^2 - u_i^n \right). \tag{29}$$

Equation (29) is modified to include the operator splitting by splitting it into two sequential sub-stages. The first step is

$$\begin{aligned}
\Delta \tilde{E} &= \tilde{E} - E^n \\
&= \sum_i m_i \left(\frac{1}{2} (\tilde{\boldsymbol{v}}_i)^2 + \tilde{u}_i - \frac{1}{2} (\boldsymbol{v}_i^n)^2 - u_i^n \right) \\
&= \sum_i m_i \left(\Delta \tilde{\boldsymbol{v}}_i \left(\boldsymbol{v}_i^n + \frac{\Delta \tilde{\boldsymbol{v}}_i}{2} \right) + \Delta \tilde{u}_i \right) \\
&= 0,
\end{aligned} \tag{30}$$

where $\Delta \tilde{\boldsymbol{v}}_i = \Delta t (d\tilde{\boldsymbol{v}}_i/dt)$, $\Delta \tilde{u}_i = \Delta t (d\tilde{u}_i/dt) = \tilde{u}_i - u_i^n$ and the fact that $\tilde{\boldsymbol{v}}_i = \boldsymbol{v}_i^n + \Delta \tilde{\boldsymbol{v}}_i$ has been used. The second step is

$$\begin{aligned}
\Delta E &= E^{n+1} - \tilde{E} \\
&= \sum_i m_i \left(\frac{1}{2} (\boldsymbol{v}_i^{n+1})^2 + u_i^{n+1} - \frac{1}{2} (\tilde{\boldsymbol{v}}_i)^2 - \tilde{u}_i \right) \\
&= \sum_i m_i \left(\Delta \check{\boldsymbol{v}}_i \left(\tilde{\boldsymbol{v}}_i + \frac{\Delta \check{\boldsymbol{v}}_i}{2} \right) + \Delta \check{u}_i \right) \\
&= 0,
\end{aligned} \tag{31}$$

where $\Delta \check{\boldsymbol{v}}_i = \Delta t (d\check{\boldsymbol{v}}_i/dt)$, $\Delta \check{u}_i = \Delta t (d\check{u}_i/dt) = u_i^{n+1} - \tilde{u}_i$ and similarly $\boldsymbol{v}_i^{n+1} = \tilde{\boldsymbol{v}}_i + \Delta \check{\boldsymbol{v}}_i$. The deviatoric part of the split energy equation is then modified to give

$$\frac{D\tilde{u}_i}{Dt} = \sum_j m_j \left(\frac{\boldsymbol{\tau}_i + \boldsymbol{\tau}_j}{\rho_i \rho_j} \right) (\bar{\boldsymbol{v}}_{ij} - \dot{\boldsymbol{x}}_i) \cdot \nabla_i W_{ij}, \tag{32}$$

where the substitution $\bar{\boldsymbol{v}}_{ij} = 0.5(\boldsymbol{v}_i + \boldsymbol{v}_j)$ is made and $\dot{\boldsymbol{x}}_i = \boldsymbol{v}_i + \Delta \tilde{\boldsymbol{v}}_i/2$ is the time-centered velocity. The use of this time-centering ensures that energy is conserved exactly in the first-step of the time-split integration procedure. This can be shown by substituting $\dot{\boldsymbol{x}}_i$ and (32) into (30) to give

$$\begin{aligned}
\Delta \tilde{E} &= \sum_i m_i \left(\Delta \tilde{\boldsymbol{v}}_i \dot{\boldsymbol{x}}_i + \Delta \tilde{u}_i \right) \\
&= \Delta t \sum_i \sum_j \frac{\bar{\boldsymbol{v}}_{ij} m_i m_j}{\rho_i \rho_j} (\boldsymbol{\tau}_i + \boldsymbol{\tau}_j) \cdot \nabla_i W_{ij} \\
&= 0.
\end{aligned} \tag{33}$$

For the hydrodynamic part of the split energy equation the method of Inutsuka [12] is followed;

$$\frac{D\check{u}_i}{Dt} = -2\sum_j m_j \left(\frac{P^*_{ij}}{\rho_i\rho_j}\right)\left(\tilde{v}^*_{ij}\boldsymbol{e}_{ij} - \tilde{\dot{\boldsymbol{x}}}_i\right)\cdot\nabla_i W_{ij}, \tag{34}$$

where $\tilde{\dot{\boldsymbol{x}}}_i = \tilde{\boldsymbol{v}}_i + \Delta\check{\boldsymbol{v}}_i/2$ is the time-centered velocity in the second-step of the split integration procedure. Again, this use of the time-centering ensures that energy is conserved exactly in the second step of the split integration procedure, which can be shown by substituting $\tilde{\dot{\boldsymbol{x}}}_i$ and (34) into (31) to give

$$\begin{aligned}\Delta E &= \sum_i m_i\left(\Delta\check{\boldsymbol{v}}_i\tilde{\dot{\boldsymbol{x}}}_i + \Delta\check{u}_i\right)\\ &= -2\Delta t\sum_i\sum_j \frac{m_i m_j P^*_{ij}\tilde{v}^*_{ij}\boldsymbol{e}_{ij}}{\rho_i\rho_j}\cdot\nabla_i W_{ij}\\ &= 0.\end{aligned}\tag{35}$$

In the case of an inviscid fluid ($\boldsymbol{\tau} = \mathbf{0}$) the time centering of Inutsuka [12] is recovered as $\tilde{\boldsymbol{v}}_i = \mathbf{0}$. It is worth noting that, if the total energy is used as an indicator of the solution quality, for example, then the exactly conservative scheme presented above may not advantageous. An appropriate system of units should be selected such that round-off error is minimized.

4 NUMERICAL TESTS

The chosen tests have exact solutions for comparison. From hereon in we refer to the first-order Godunov SPH scheme of Parshikov *et al.* [23] as *PM*, the new time-split Godunov SPH scheme as *TS* and the standard artificial viscosity scheme (with Monaghan-type artificial viscosity [22] and damping parameters $\alpha = \beta = 1$) as *AV*. In the *AV* scheme the second-order leap-frog integration scheme is used [19]. In this work the Godunov SPH scheme of Parshikov *et al.* [23] was implemented in one dimension only. In all cases the time-step was controlled by the CFL number of 0.5 and the initial smoothing length scaling factor was 1.2.

4.1 1D flyer-plate

This example comes from [5] and consists of an impact of a high-velocity elastic-perfectly-plastic material with another identical material which is at rest. The impact produces an elastic precursor wave followed by a plastic shock-wave. An isothermal Mie-Grüneisen Equation of State (EOS) is used (as the Grüneisen coefficient is zero), defined as [5]

$$P(\rho) = \frac{\rho_0 c_0^2\zeta}{1-(S_1-1)\zeta}, \tag{36}$$

where $\zeta = \rho/\rho_0 - 1$. The material properties are given as $\rho_0 = 6.1$ g/cm^3, $c_0 = 0.5077$ cm/μs, $S_1 = 1.201$, $\mu = 0.481$ MBar and $Y_0 = 0.025$ MBar [5]. The initial conditions are given in Table 1. The solution is integrated until $t = 0.5\mu$s and the domain is over $0 \le x \le 1$ with the left hand side defined as $x \le 0.5$. Figure 1 shows the non-dimensional results using the different schemes 100 (equally spaced) particles in the domain against the exact solution [5].

$\tau_l = 0$	$\tau_r = 0$
$\rho_l = \rho_0$	$\rho_r = \rho_0$
$v_l = 0.060281$ cm$/\mu$s	$v_r = 0$

Table 1: Initial conditions for the flyer-plate impact example (from [5]).

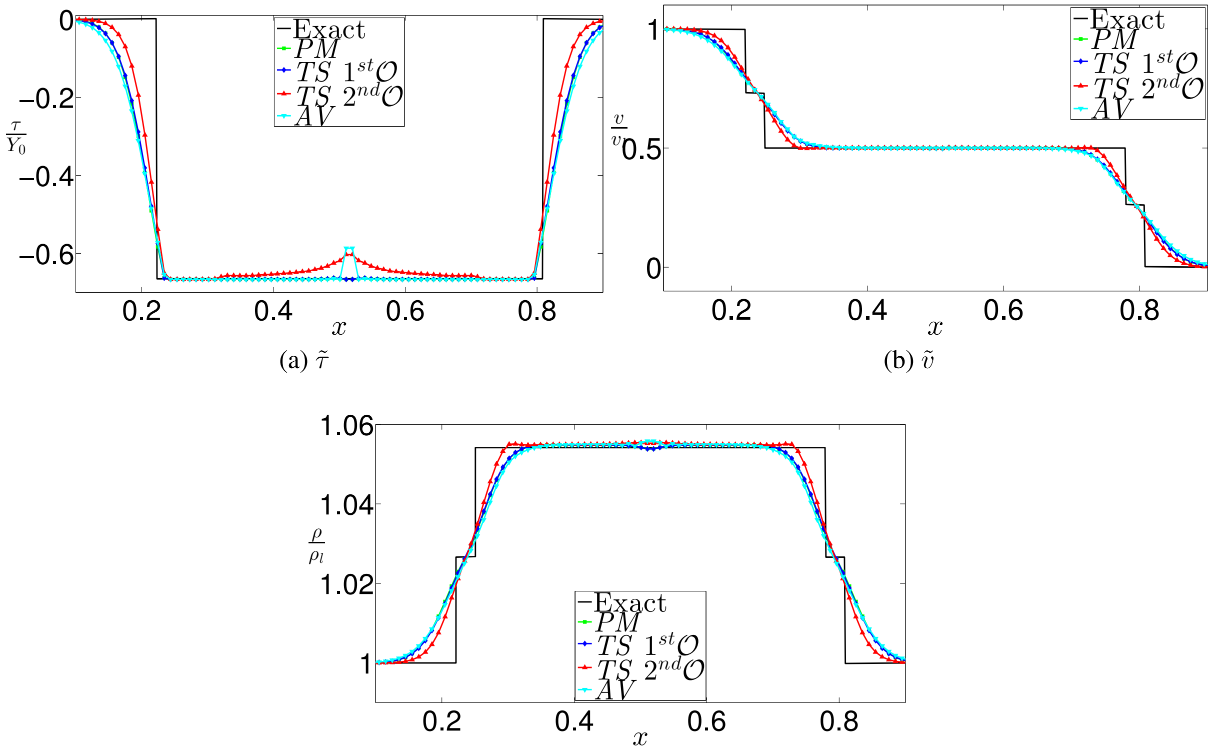

(a) $\tilde{\tau}$ (b) $\tilde{v}$ (c) $\tilde{\rho}$

Figure 1: Results of the flyer-plate example using the different schemes for an initial inter-particle spacing of $\Delta x = 0.01$ cm. The exact solution [5] is given by the black line.

It can be seen from Figure 1 that the results from the *PM*, first order *TS* and *AV* schemes are similar, however the second-order *TS* scheme shows a more accurate description around the discontinuities in field variables. In the second-order *TS* scheme there is an error in the stress field around the contact discontinuity. The *AV* scheme shows a similar but more localised error. The difference in total energy for the different schemes is shown in Table 2.

Scheme	$\% \, \Delta E_{tot}$
PM	2.34
TS 1^{st} $\mathcal{O}$	1.48×10^{-8}
TS 2^{nd} $\mathcal{O}$	1.48×10^{-8}
AV	1.51

Table 2: Percentage errors in total energy for the flyer-plate impact example using the different schemes.

4.2 2D Collapsing ring

This problem involves the collapse of an axi-symmetrical beryllium ring which was first proposed by Howell and Ball [10] . The problem has an analytical solution [10] which derives from incompressible theory and the reduction to one-dimension. A detailed derivation of the analytical solution is presented in [10] . The analytical solution predicts a stopping radius at which all the initial kinetic energy is dissipated by irreversible plastic deformation into internal energy. Howell and Ball use the Osborne equation of state, but the analytical solution is independent of the pressure, therefore, as suggested in [24], the Mie-Grüneisen equation of state of the form

$$P(\rho, u) = \frac{\rho_0 c_0^2 (\eta - 1) \left(\eta - \frac{1}{2}\Gamma_0 (\eta - 1)\right)}{\left(\eta - S_1 (\eta - 1)\right)^2} + \rho_0 \Gamma_0 u, \tag{37}$$

where $\eta = \rho/\rho_0$ is used with parameters proposed in [24] of $\rho_0 = 1845.0$ kg/m^3, $c_0 = 12870.0$ m/s, $S_1 = 1.124$ and $\Gamma_0 = 2.0$. The elastic-perfectly-plastic constitutive model is used with $\mu = 15.1$ GPa and $Y_0 = 330.0$ MPa. As mentioned in [10], for the test to be successful, the circumferential symmetry must be preserved and the stopping radii must converge towards the analytical solution. The initial velocity field is defined as

$$\boldsymbol{v}_i = -v_0 \frac{R_1}{r_i} \boldsymbol{e}_i, \tag{38}$$

where $v_0 = 417.1$ m/s, $R_1 = 0.08$ m is the inner radius in the initial configuration, r_i is the distance of particle i from the origin and $\boldsymbol{e}_i$ is the unit vector of the particle position. The analytical solution [10] predicts the inner and outer stopping radii to be 0.05 m and 0.0781 m respectively. As the *PM* scheme was implemented in one dimension only the results of the *TS* schemes are compared with the *AV* scheme using two different resolutions ($n_p = 8012$ and $n_p = 23,506$). In this example the two-shock approximate Riemann solver [7] is used in the *TS* scheme. The solution was integrated until $t = 130\mu$s which was just after the cessation of plastic deformation in each case. The final configurations for the lower resolution using the first and second order *TS* schemes and *AV* scheme, coloured by the effective plastic strain and τ_{xy} deviatoric stress, are shown in Figure 2. It can be seen that the stress field is noisy in the *AV* scheme suggesting that the dynamics of the deformation are not being properly predicted; a similar result is found for the other field variables.

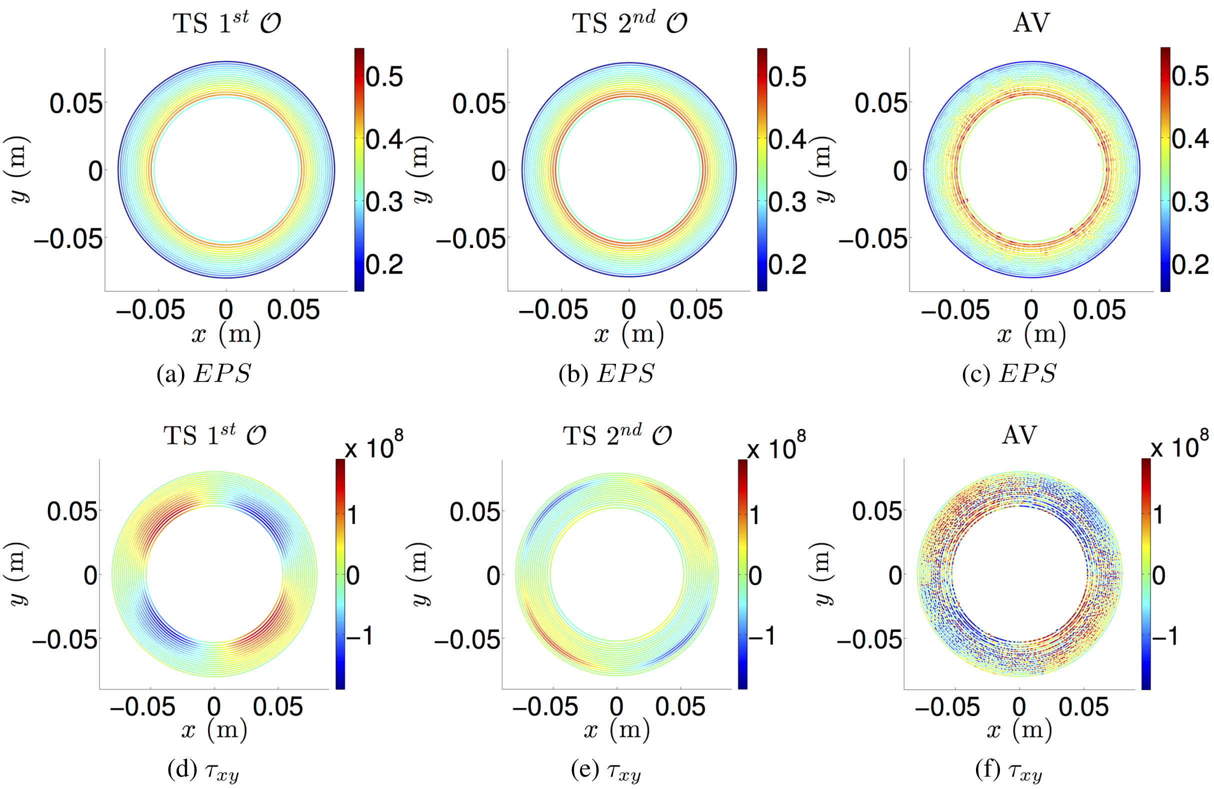

Figure 2: The final configurations (at $t = 130\mu$s) for the lower resolution ($n_p = 8012$) ring collapse example using the different SPH schemes. The units of the colourmap for the τ_{xy} results are in Pa.

The difference in the colourmap for the τ_{xy} results between the 1^{st} $\mathcal{O}$ and 2^{nd} $\mathcal{O}$ *TS* schemes is due to the difference in phase of the elastic oscillation after the cessation of yielding. The results for the finest resolution are shown in Figure 3.

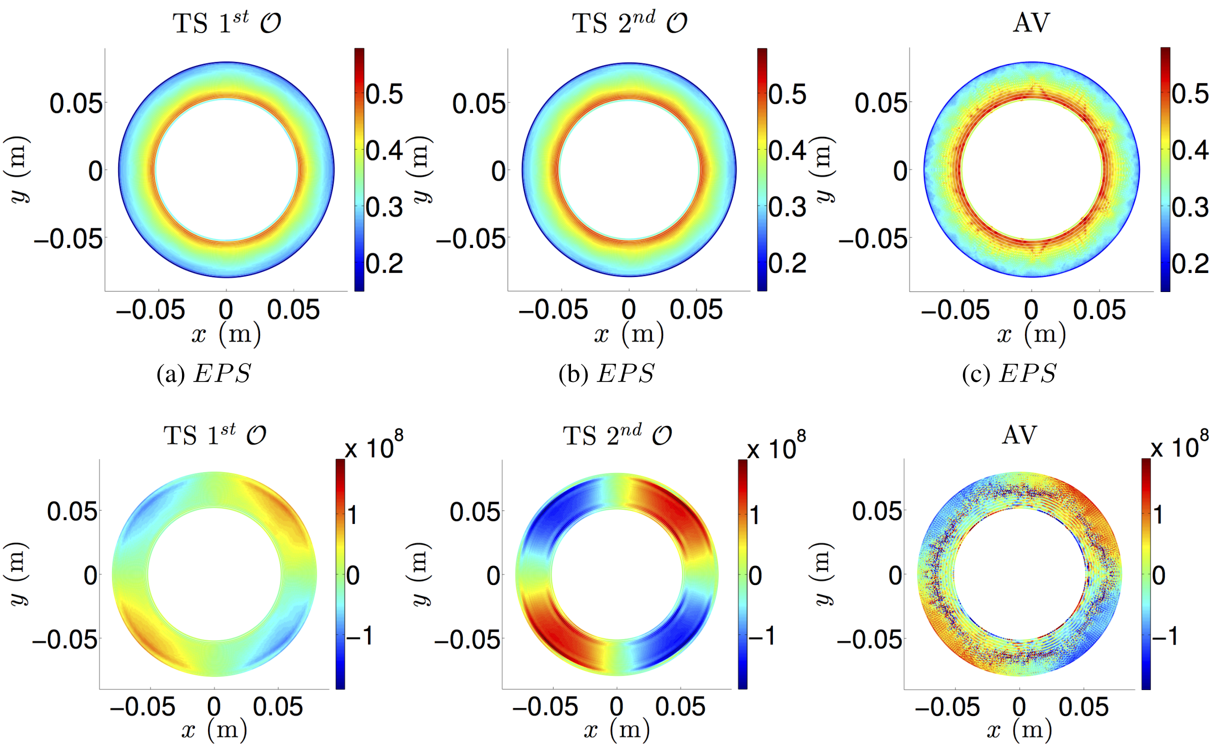

(a) EPS (b) EPS (c) EPS

(d) τ_{xy} (e) τ_{xy} (f) τ_{xy}

Figure 3: The final configurations (at $t = 130\mu$s) for the higher resolution ($n_p = 23,506$) ring collapse example using the different SPH schemes. The units of the colourmap for the τ_{xy} results are in Pa.

The particle configuration of the *AV* scheme shows a considerable amount of disorder and the inner ring of particles have lost their circumferential symmetry. Therefore, according to the criteria of [10] , the *AV* scheme fails this test. For this reason only the inner and outer radii of the *TS* schemes are compared with the exact solution; this is shown as a function of time in Figure 4. The non-dimensional internal, kinetic and total energies for each of the schemes are shown in Figure 5. The percentage change in total energy (at $t = 130\mu$s) for each of the schemes is shown in Table 3. As the error in total energy in the *TS* scheme is due only to machine round-off, the error may be minimized by an appropriate choice of units.

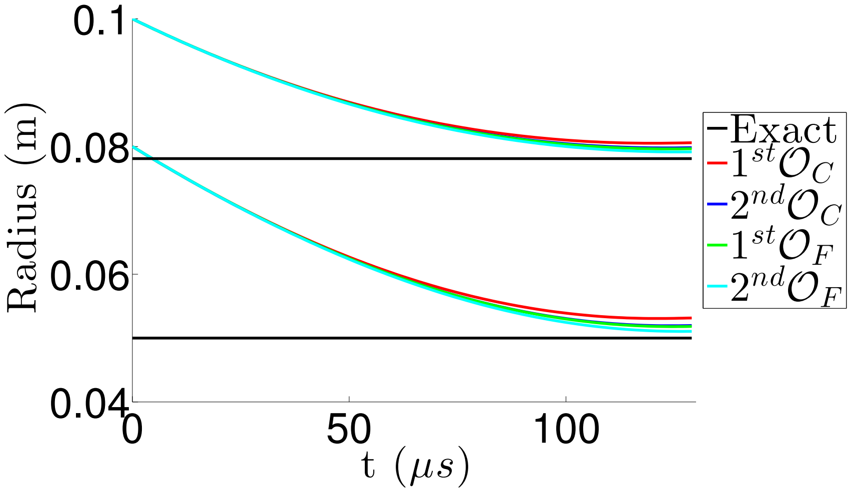

Figure 4: The inner and outer radii of the collapsing ring as a function of time using the *TS* scheme. The subscripts C and F in the legend mean the coarse and fine resolution respectively.

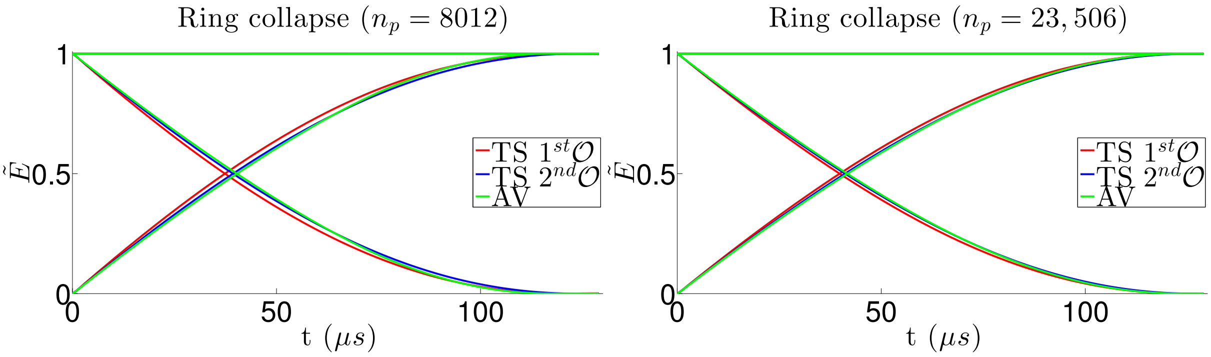

(a) $n_p = 8012$ (b) $n_p = 23,506$

Figure 5: The non-dimensional internal (increasing), kinetic (decreasing) and total energies using the *TS* and *AV* schemes for the collapsing ring case.

Scheme	% ΔE_{tot} ($n_p = 8012$)	% ΔE_{tot} ($n_p = 23,506$)
TS 1st $\mathcal{O}$	3.04×10^{-2}	2.75×10^{-11}
TS 2nd $\mathcal{O}$	6.67×10^{-4}	2.09×10^{-7}
AV	1.12×10^{-1}	2.55×10^{-4}

Table 3: Percentage errors in total energy for the ring-collapse example using the different schemes. Note that the results using only the *AV* and *TS* schemes are shown as the *PM* scheme was implemented in one-dimension only.

5 APPLICATION

An impact of a steel projectile on a silicon carbide tile is simulated using the *AV* and first and second-order *TS* schemes in 2D plane strain. The steel is described using the Johnson-Cook [13] constitutive model and the Mie-Grüneisen EOS of the form in equation (37) and the silicon carbide uses the piece-wise linear JH1 ceramic-damage model [14] with a polynomial EOS of the form (with bulking turned off)

$$P(\rho) = k_1\zeta + k_2\zeta^2 + k_3\zeta^3. \tag{39}$$

The Johnson-Cook flow-stress is purely phenomenological, includes terms to take account of the competition between thermal softening and strain hardening and takes the form

$$\sigma_y\left(\epsilon_p, \dot{\epsilon_p}, T\right) = \left(A + B\left(\epsilon_p^n\right)\right)\left[1 + C\ln\left(\frac{\dot{\epsilon_p}}{\dot{\epsilon_0}}\right)\right]\left[1 - \left(\frac{T - T_0}{T_m - T_0}\right)^m\right], \tag{40}$$

where A, B, C, m and n are user-defined parameters and ϵ_p is the plastic strain, $\dot{\epsilon_p}$ is the plastic strain rate, $\dot{\epsilon_0}$ is the reference strain rate, T is the current temperature, T_m is the melting temperature and T_0 is the reference temperature (in degrees Kelvin).

In the JH1 ceramic damage model the yield surface of the material is based upon two piece-wise linear curves; one represents the "intact" strength σ_i and one represents the "damaged" strength σ_d. The material damage is represented by a scalar variable D, where $0 \leq D \leq 1$. When $D < 1$ the strength is represented by the intact strength curve σ_i. A schematic of the JH1 constitutive model is shown in Figure 6. When $D = 1$ the material instantly fails and the

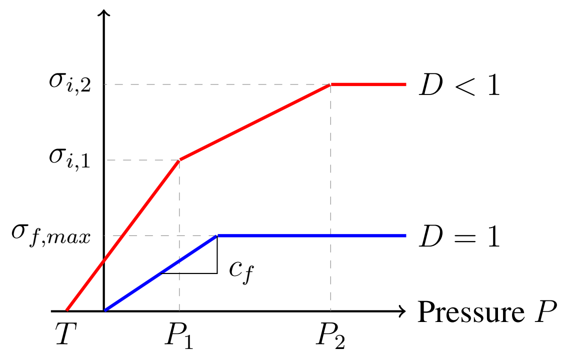

Figure 6: Schematic of JH1 constitutive model.

failed strength curve σ_d is followed. Note that when $D = 1$, the failure strength is only followed for compressive stresses. A gradual softening of the material is allowed in the JH2 constitutive equation [15], however it was found that some fundamental behaviours, such as interface dwell, were not captured accurately with a gradually softening material model [16]. The scalar damage variable D is allowed to increase monotonically as a function of the incremental plastic strain $\Delta\epsilon_p$ and failure stain ϵ_f through

$$D = \sum_t \frac{\Delta\epsilon_p}{\epsilon_f}. \tag{41}$$

The failure strain itself is a linear function of the hydrostatic pressure and is obtained by the interpolation of the line in Figure 7. In the case where $P = T$, the damage variable is set to unity. The material parameters for the silicon carbide target and steel projectile are given in Table 4.

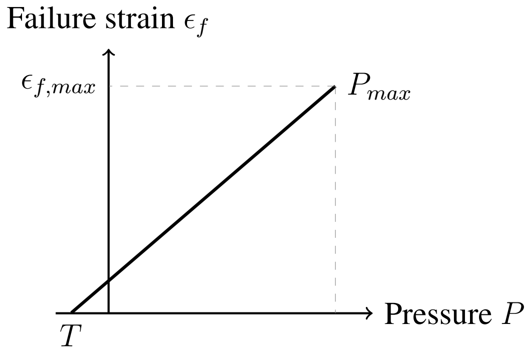

Figure 7: Schematic of JH1 failure strain curve.

SiC EOS Parameter	*Value*	*Steel EOS Parameter*	*Value*
ρ_0	3215 kg/m^3	ρ_0	7903 kg/m^3
k_1	2.2 MBar	S_1	1.4933
k_2	3.61 MBar	Γ_0	2.2
k_3	0	c_0	4.552 km/s
SiC JH1 Parameter	*Value*	*Steel JC Parameter*	*Value*
μ	1.93 MBar	μ	74.8 GPa
$\sigma_{i,1}$	7.1 GPa	A	300.0 MPa
P_1	2.5 GPa	B	1000.0 MPa
$\sigma_{i,2}$	12.2 GPa	C	0.07
P_2	10.0 GPa	M	1.0
$\sigma_{f,max}$	1.3 GPa	N	0.65
c_f	0.4	T_0	298°K
T	-750.0 MPa	T_m	1673°K
$\epsilon_{f,max}$	0.8	c_p	440 J/Kg K
P_{max}	99.75 GPa	χ	0.9
C	0.009	—	—

Table 4: Material parameters for the Johnson-Cook flow stress and Johnson-Holmquist ceramic damage models, from [26].

It is important to note that, in the time-split integration scheme, because the dilatational and deviatoric components are separate, a modification to the dilatational step must be made to reflect the failure model in the constitutive equation. In the case of either of the two interacting particles possessing a damage variable of unity the first-order Godunov scheme is recovered; no linear reconstruction or slope limiting is applied. The following algorithm is proposed for use between each interaction pair: Algorithm 1 ensures that hydrostatic tension is not sustained between damaged particles. It can be thought of as an extension to the limiting procedure in light of the constitutive equation used and the time-splitting procedure which separates the dilatational and deviatoric responses.

The projectile and target are rectangular and have dimensions of $l_p = 2$ cm, $w_p = 1$ cm and $l_t = 3$ cm, $w_t = 10$ cm respectively. In total there are $51,842$ equally spaced particles in the domain. The projectile impacts the target with a velocity of 800 m/s. The results (using the

Algorithm 1 Modification to Riemann solution for instantaneous failure

```
if D_i = 1 ∧ D_j = 1 then                                  ▷ Both particles fully damaged
    P_R ← P_i, P_L ← P_j        ⎫
    v_R ← v_i^R, v_L ← v_j^R    ⎬ No reconstruction
    ρ_R ← ρ_i, ρ_L ← ρ_j        ⎭
    if P_i < 0 then                                        ▷ Tension not allowed
        P_i ← 0
    end if
    if P_j < 0 then                                        ▷ Tension not allowed
        P_j ← 0
    end if
    Calculate P*_ij, v*_ij                                 ▷ Call Riemann solver
    if P*_ij < 0 then                                      ▷ No tension allowed
        P*_ij ← 0
    end if
else if D_i = 1 ∨ D_j = 1 then                             ▷ One or more particle fully damaged
    P_R ← P_i, P_L ← P_j        ⎫
    v_R ← v_i^R, v_L ← v_j^R    ⎬ No reconstruction
    ρ_R ← ρ_i, ρ_L ← ρ_j        ⎭
    if D_i = 1 then                                        ▷ If particle i damaged
        if P_i < 0 then                                    ▷ Tension not allowed
            P_i ← 0
        end if
    end if
    if D_j = 1 then                                        ▷ If particle j damaged
        if P_j < 0 then                                    ▷ Tension not allowed
            P_j ← 0
        end if
    end if
    Calculate P*_ij, v*_ij                                 ▷ Call Riemann solver
    if P*_ij < 0 then                                      ▷ No tension allowed
        P*_ij ← 0
    end if
else                                                       ▷ Both particles undamaged
    Calculate P*_ij, v*_ij                                 ▷ Call Riemann solver
end if
```

1st $\mathcal{O}$ *TS*, 2nd $\mathcal{O}$ *TS* and *AV* schemes) of damage field after 5, 10 and 15μ are shown in Figure 8. It can be seen from Figure 8 that the damage fields using the first order and second-order *TS* schemes are different to that using the *AV* scheme, however the second-order *TS* scheme shows the most similar damage field to the *AV* scheme. A region of spall is predicted near the back-face of the target in each case. Figure 9 shows the x component of the velocity for the three different schemes; it can be seen that the second-order *TS* scheme predicts the highest spall velocity.

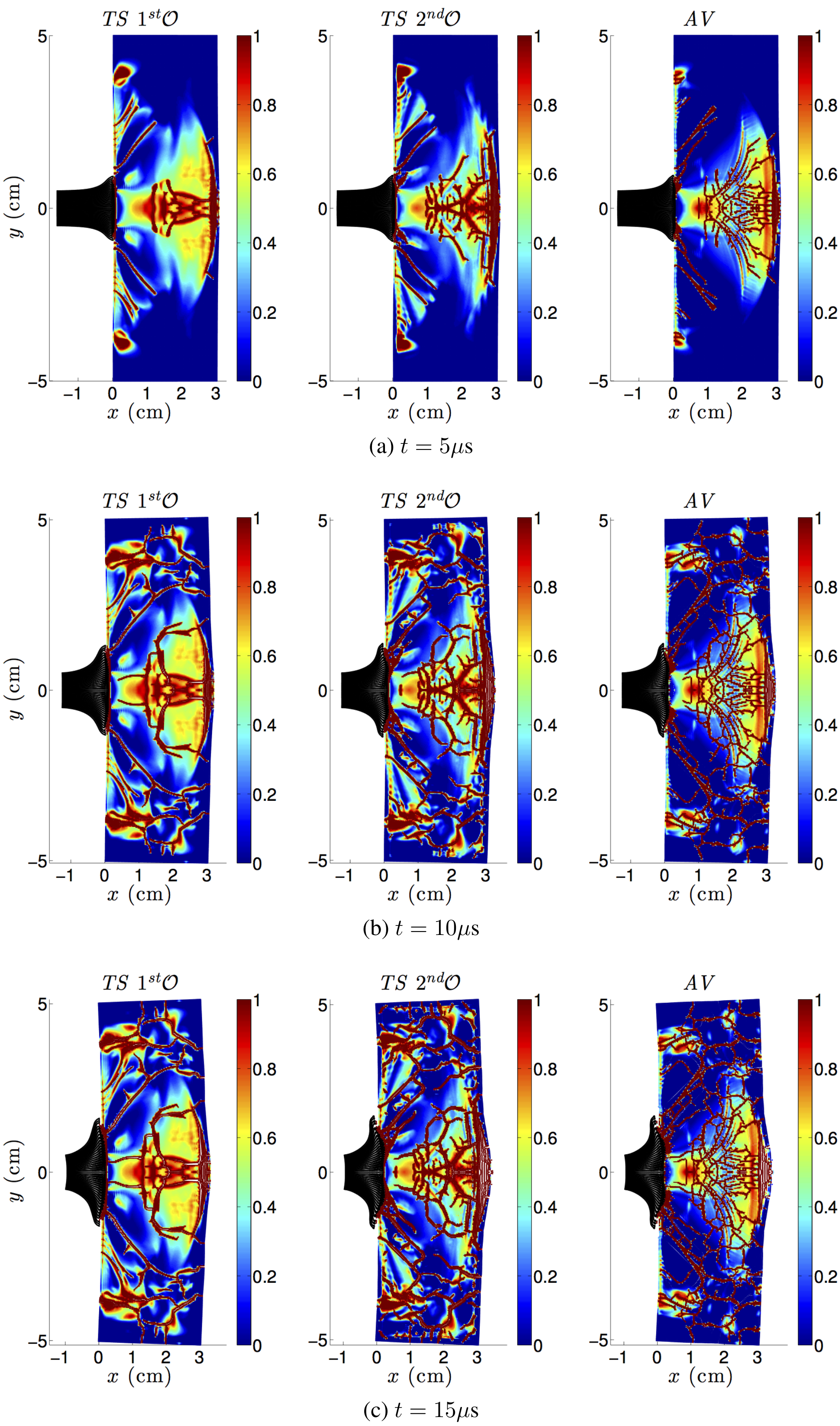

Figure 8: The results of the steel-SiC impact simulation showing scalar damage field for the three schemes at different instances. The steel projectile is shown in black.

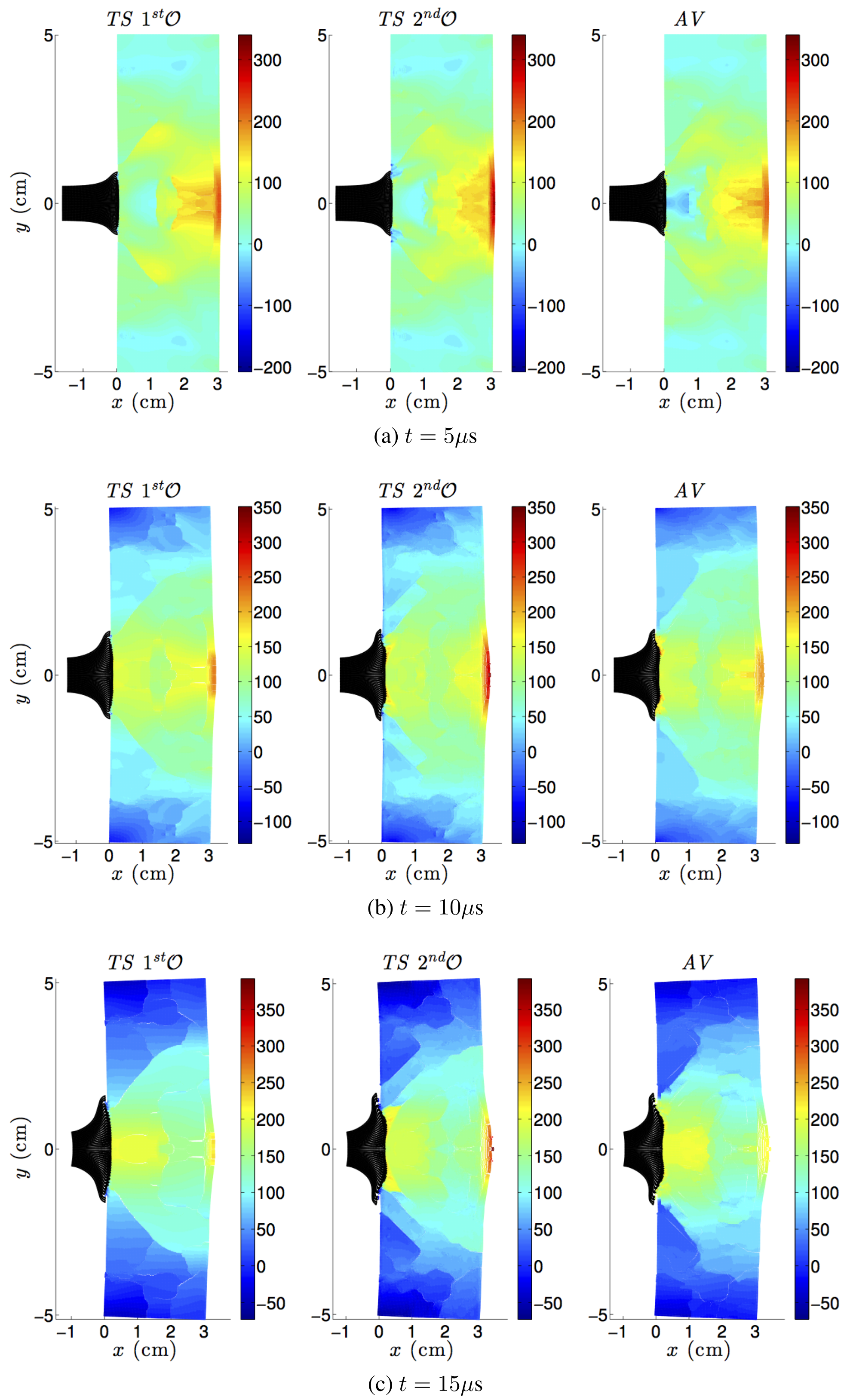

Figure 9: The results of the steel-SiC impact simulation showing x component of the velocity field for the three schemes at different instances. The steel projectile is shown in black.

6 CONCLUSIONS

An extension of the Godunov SPH method of Parshikov *et al.* [23] to second-order has been described for materials with strength. The method relies on the decomposition of the Cauchy stress tensor to its constituent hydrodynamic and deviatoric parts, which are then used within a Lie-Trotter splitting algorithm to integrate the continuum equations sequentially in time. The splitting procedure facilitates the second-order reconstruction of the left and right Riemann-states, as only the longitudinal wave system needs to be solved. In the two-dimensional ring collapse example, it is shown that, in contrast to the *AV* scheme, the *TS* schemes display less particle disorder. This may have the advantageous side effect of enhancing the relative accuracy of the particle approximation of the gradient. The *TS* scheme, however, inherits the kernel instability intrinsic to the SPH method [29] (when using an Eulerian kernel [2]), as the same particle approximation method is used to calculate the derivatives as in the standard *AV* scheme. Further accuracy may be added to the spatial integration procedure by adopting a mixed kernel and kernel gradient correction procedure [17, 18, 34]. An algorithm was proposed to incorporate, into the *TS* scheme, a constitutive model based on continuum damage mechanics such that the scheme could be used to simulate brittle materials. The *TS* scheme is more computationally expensive than both the *AV* and *PM* schemes (the 2^{nd} $\mathcal{O}$ scheme is approximately $2.5\times$ more expensive than the *AV* scheme), however advances in massively parallel GPU computing techniques may reduce this burden to the point where the *TS* scheme is practical [20, 36, 31, 6].

REFERENCES

[1] D. S. Balsara. von-Neumann analysis of smoothed particle hydrodynamics - suggestions for optimal algorithms. *Journal of Computational Physics*, 121(1):357–372, 1995.

[2] T. Belytschko, Y. Krongauz, D. Organ, M. Fleming, and P. Krysl. Meshless methods: An overview and recent developments. *Computer Methods in Applied Mechanics and Engineering*, 139(1-4):3 – 47, 1996.

[3] J. Bonet, S. Kulasegaram, M. Rodriguez-Paz, and M. Profit. Variational formulation for the smooth particle hydrodynamics (SPH) simulation of fluid and solid problems. *Computer Methods in Applied Mechanics and Engineering*, 193(12-14):1245 – 1256, 2004.

[4] L. Cullen and W. Dehnen. Inviscid smoothed particle hydrodynamics. *Monthly Notices of the Royal Astronomical Society*, 408(2):669–683, 2010.

[5] V. A. Dobrev, T. E. Ellis, T. V. Kolev, and R. N. Rieben. High-order curvilinear finite elements for axisymmetric lagrangian dynamics. *Journal of Computational Physics*, (0):– , 2013.

[6] J. M. Domanguez, A. J. Crespo, and M. Gomez-Gesteira. Optimization strategies for cpu and gpu implementations of a smoothed particle hydrodynamics method. *Computer Physics Communications*, 184(3):617 – 627, 2013.

[7] J. K. Dukowicz. A general, non-iterative riemann solver for Godunov's method. *Journal of Computational Physics*, 61(1):119 – 137, 1985.

[8] S. K. Godunov. Difference methods for the numerical calculation of the equations of fluid dynamics. *Math Sbornik*, 47:221–306, 1959.

[9] L. Hernquist and N. Katz. TREESPH - a unification of SPH with the hierarchical tree method. *Astrophysical Journal Supplement*, 70:419–446, 1989.

[10] B. P. Howell and G. J. Ball. A free-lagrange augmented Godunov method for the simulation of elastic plastic solids. *Journal of Computational Physics*, 175(1):128–167, 2002.

[11] S.-I. Inutsuka. Godunov-type SPH. *Memorie della Società Astronomia Italiana*, 65:1027–1031, 1994.

[12] S.-I. Inutsuka. Reformulation of smoothed particle hydrodynamics with Riemann solver. *Journal of Computational Physics*, 179:238–267, 2002.

[13] G. R. Johnson and W. H. Cook. A constitutive model and data for metals subjected to large strains, high strain rates and high temperatures. In *Proceedings of the 7th International Symposium on Ballistics*, 1983.

[14] G. R. Johnson and T. J. Holmquist. *A computational constitutive model for brittle materials subjected to large strains, high strain rates and high pressures*. CRC Press, 1992. editors M. A. Meyers, L. E. Murr and K. P. Staudhammer and Marcel Dekker Inc.

[15] G. R. Johnson and T. J. Holmquist. An improved computational constitutive model for brittle materials. *AIP Conference Proceedings*, 309(1):981–984, 1994.

[16] G. R. Johnson, T. J. Holmquist, and S. R. Beissel. Response of aluminum nitride (including a phase change) to large strains, high strain rates, and high pressures. *Journal of Applied Physics*, 94(3):1639–1646, 2003.

[17] N. Lanson and J. P. Vila. Renormalized meshfree schemes I: consistency, stability, and hybrid methods for conservation laws. *SIAM Journal on Numerical Analysis*, 46(4):1912–1934, 2008.

[18] N. Lanson and J. P. Vila. Renormalized meshfree schemes II: convergence for scalar conservation laws. *SIAM Journal on Numerical Analysis*, 46(4):1935–1964, 2008.

[19] G. R. Liu and M. B. Liu. *Smoothed Particle Hydrodynamics, a meshfree particle method*. World Scientific, 2003.

[20] B. long Wang and H. Liu. Application of sph method on free surface flows on gpu. *Journal of Hydrodynamics, Ser. B*, 22(5, Supplement 1):912 – 914, 2010.

[21] J. J. Monaghan. Smoothed particle hydrodynamics. *Reports on Progress in Physics*, 68:1703–1759, 2005.

[22] J. J. Monaghan and R. A. Gingold. Shock simulation by the particle method SPH. *Journal of Computational Physics*, 52:374–389, 1983.

[23] A. N. Parshikov and S. A. Medin. Smoothed particle hydrodynamics using interparticle contact algorithms. *Journal of Computational Physics*, 180(1):358–382, 2002.

[24] M. Pierre-Henri, R. Abgrall, J. Breil, R. Loubère, and B. Rebourcet. A nominally second-order cell-centered Lagrangian scheme for simulating elastic-plastic flows on two-dimensional unstructured grids. Rapport de recherche RR-7975, INRIA, May 2012.

[25] D. J. Price. Smoothed particle hydrodynamics and magnetohydrodynamics. *Journal of Computational Physics*, 231(3):759 – 794, 2012.

[26] X. Quan, R. Clegg, M. Cowler, N. Birnbaum, and C. Hayhurst. Numerical simulation of long rods impacting silicon carbide targets using JH-1 model. *International Journal of Impact Engineering*, 33(1-12):634 – 644, 2006.

[27] J. I. Read and T. Hayfield. SPHS: Smoothed Particle Hydrodynamics with a higher order dissipation switch. *Monthly Notices of the Royal Astronomical Society*, 2011. In press.

[28] A. Shaw and S. R. Reid. Heuristic acceleration correction algorithm for use in SPH computations in impact mechanics. *Computational Methods in Applied Mechanics and Engineering*, 198(128):3962–3974, 2009.

[29] J. Swegle, J. Hicks, and S. Attaway. Smoothed particle hydrodynamics stability analysis. *Journal of Computational Physics*, 116:123–134, 1995.

[30] E. F. Toro. *Riemann Solvers and Numerical Methods for Fluid Dynamics: A Practical Introduction*. Springer, 1999.

[31] D. Valdez-Balderas, J. M. Domanguez, B. D. Rogers, and A. J. Crespo. Towards accelerating smoothed particle hydrodynamics simulations for free-surface flows on multi-gpu clusters. *Journal of Parallel and Distributed Computing*, (0):–, 2012.

[32] B. van Leer. Towards the ultimate conservative difference scheme - a second-order sequel to Godunov's method. *Journal of Computational Physics*, 32(1):101–136, 1979.

[33] J. Vila. On particle weighted methods and smooth particle hydrodynamics. *Mathematical Models and Methods in Applied Sciences*, 09(02):1935–1964, 1999.

[34] J. P. Vila. SPH renormalized hybrid methods for conservation laws: Applications to free surface flows. In M. Griebel, M. A. Schweitzer, T. J. Barth, M. Griebel, D. E. Keyes, R. M. Nieminen, D. Roose, and T. Schlick, editors, *Meshfree Methods for Partial Differential Equations II*, volume 43 of *Lecture Notes in Computational Science and Engineering*, pages 207–229. 2005.

[35] M. L. Wilkins. *Computer Simulation of Dynamic Phenomena*. Springer, 1998.

[36] Q. Xiong, B. Li, and J. Xu. Gpu-accelerated adaptive particle splitting and merging in sph. *Computer Physics Communications*, (0):–, 2013.